

# COMPACT QUIESCENT GALAXIES AT INTERMEDIATE REDSHIFTS<sup>1,2</sup>

LI-YEN HSU, ALAN STOCKTON, AND HSIN-YI SHIH<sup>3</sup>

Institute of Astronomy, University of Hawaii, 2680 Woodlawn Drive, Honolulu, HI 96822, USA

*Accepted to The Astrophysical Journal*

## ABSTRACT

From several searches of the area common to the Sloan Digital Sky Survey and the United Kingdom Infrared Telescope Infrared Deep Sky Survey, we have selected 22 luminous galaxies between  $z \sim 0.4$  and  $z \sim 0.9$  that have colors and sizes similar to those of the compact quiescent galaxies at  $z > 2$ . By exploring structural parameters and stellar populations, we found that most of these galaxies actually formed most of their stars at  $z < 2$  and are generally less compact than those found at  $z > 2$ . Several of these young objects are disk-like or possibly prolate. This lines up with several previous studies which found that massive quiescent galaxies at high redshifts often have disk-like morphologies. If these galaxies were to be confirmed to be disk-like, their formation mechanism must be able to account for both compactness and disks. On the other hand, if these galaxies were to be confirmed to be prolate, the fact that prolate galaxies do not exist in the local universe would indicate that galaxy formation mechanisms have evolved over cosmic time. We also found five galaxies forming over 80% of their stellar masses at  $z > 2$ . Three of these galaxies appear to have been modified to have spheroid-like morphologies, in agreement with the scenario of “inside-out” buildup of massive galaxies. The remaining galaxies, SDSS J014355.21+133451.4 and SDSS J115836.93+021535.1, have truly old stellar populations and disk-like morphologies. These two objects would be good candidates for nearly unmodified compact quiescent galaxies from high redshifts that are worth future study.

*Subject headings:* galaxies: formation – galaxies: kinematics and dynamics – galaxies: stellar content – galaxies: structure

## 1. INTRODUCTION

The structural evolution of massive galaxies over cosmic time provides constraints on galaxy formation models. In the local universe, galaxies with stellar masses greater than  $10^{11} M_{\odot}$  are mostly early-type galaxies (Baldry et al. 2004; Buitrago et al. 2013), which usually have old stellar populations and large sizes. However, many recent studies have found evidence that massive galaxies at  $z > 2$  showing little or no recent star formation are generally very compact, with effective radii  $R_e < 2$  kpc (e.g., Stockton et al. 2004; Daddi et al. 2005; Trujillo et al. 2006, 2007; Toft et al. 2007; van Dokkum et al. 2008; Buitrago et al. 2008; Damjanov et al. 2009; Bruce et al. 2012; van der Wel et al. 2014). Proposed mechanisms to create such compact galaxies from star-forming progenitors generally involve violent, dynamical processes such as gas-rich mergers (Hopkins et al. 2006) or dynamical instabilities fed by cold streams (Dekel et al. 2009).

Because these compact and quiescent galaxies are extremely rare in the present-day universe (e.g., Trujillo et al. 2009; Taylor et al. 2010), significant size growth must have taken place over the past billions of years, and stochastic events such as major mergers cannot be the dominant mechanisms (e.g., Bezanson et al. 2009; López-Sanjuan et al. 2010). It has been proposed that minor mergers (e.g., Khochfar & Silk 2006; Naab et al. 2009) or “puffing-up” driven by active galactic nuclei (AGN) feedback (e.g., Fan et al. 2008, 2010) have turned these high-redshift compact galaxies into

present-day ellipticals. Most of the recent studies, however, favor the former mechanism, proposing the so-called inside-out buildup of present-day massive galaxies (e.g., Bezanson et al. 2009; Hopkins et al. 2009a; van Dokkum et al. 2010; Trujillo et al. 2011; van de Sande et al. 2013). In this scenario, the high-redshift compact galaxies become the cores of the most massive local galaxies after accreting envelopes over time.

It is very difficult to study the compact quiescent galaxies at  $z > 2$  in detail because of their faintness, resulting from cosmological dimming, and their low surface brightness, due to the turnover of the redshift-angular-size-distance relation at high redshifts. As a consequence, many recent studies have focused on identifying and characterizing some similar objects at lower redshifts (e.g., Trujillo et al. 2009; Taylor et al. 2010; Stockton et al. 2010; Shih & Stockton 2011; Ferré-Mateu et al. 2012; Poggianti et al. 2013; Damjanov et al. 2013; Trujillo et al. 2014; Stockton et al. 2014), where images and spectra with high quality are accessible for studying morphologies and detailed properties such as stellar populations, kinematics and metallicities. Making use of the Sloan Digital Sky Survey (SDSS), Trujillo et al. (2009) found that the number of massive ( $M_* > 8 \times 10^{10} M_{\odot}$ ) and compact ( $r_e < 1.5$  kpc) galaxies is less than 0.03% at  $z < 0.2$ . Another search by Taylor et al. (2010) at  $0.066 < z < 0.12$  returned no candidates as massive and as compact as those identified at high redshifts. Trujillo et al. (2009), Ferré-Mateu et al. (2012) and Damjanov et al. (2013) all found young ages for the compact galaxies they identified, again suggesting that most of the high-redshift compact galaxies have already turned into large ellipticals in the local universe.

Nevertheless, the stochastic nature of merging events means that there should be a number of galaxies that formed at high redshifts that have remained unmodified until today (Quilis & Trujillo 2013). Recently Trujillo et al. (2014) and Stockton

<sup>1</sup> Some of the data presented herein were obtained at the W.M. Keck Observatory, which is operated as a scientific partnership among the California Institute of Technology, the University of California and the National Aeronautics and Space Administration. The Observatory was made possible by the generous financial support of the W.M. Keck Foundation.

<sup>2</sup> Based in part on data collected at Subaru Telescope, which is operated by the National Astronomical Observatory of Japan.

<sup>3</sup> Now at Gemini Observatory, 670 N. Aohoku Pl., Hilo, HI 96720, USA

et al. (2014) have successfully found compact galaxies that may have survived with little or no modification from the population formed at high redshifts; further morphological and kinematic studies of these objects would provide us more insight into their formation mechanisms in the early universe.

Given the rareness of compact quiescent galaxies in the local universe, it would be useful to explore intermediate redshifts, where the number density of these objects is expected to be higher. The epoch between  $z \sim 0.5$  and  $z \sim 1.0$  covers a large period of cosmic time, but it is nearly unexplored in searches for compact quiescent galaxies. In this work, we present our results of 22 compact quiescent galaxies identified between  $z \sim 0.4$  and  $z \sim 0.9$  from several searches of the area common to SDSS and the United Kingdom Infrared Telescope (UKIRT) Infrared Deep Sky Survey (UKIDSS). The paper is structured as follows. Section 2 describes our object selection and follow-up observations. The analyses and results are shown in detail in Section 3. In Section 4, we discuss our results and their implications. Section 5 summarizes our results. Throughout this paper, we assume a Chabrier (2003) initial mass functions (IMF) and the concordance  $\Lambda$ CDM cosmology with  $H_0 = 70 \text{ km s}^{-1} \text{ Mpc}^{-1}$ ,  $\Omega_M = 0.3$ , and  $\Omega_\Lambda = 0.7$ . All magnitudes used are AB magnitudes.

## 2. OBJECT SELECTION AND OBSERVATIONS

### 2.1. Object Selection

Fifteen galaxies (hereafter, sample 1) we study in this work are from several searches for compact quiescent galaxies at  $0.4 \lesssim z \lesssim 0.6$  since 2009; the other seven galaxies (hereafter, sample 2) are from a new search carried out this year for  $0.4 \lesssim z \lesssim 1.0$ . Our method for selecting objects at  $0.4 \lesssim z \lesssim 0.6$  is given in Stockton et al. (2010). In the following, we describe details of the new search performed this year.

We selected objects from the area common to UKIDSS DR9plus and SDSS DR8 for right ascensions between  $8^{\text{h}}$  and  $16^{\text{h}}$ . In order to generate the expected colors of old stellar populations, a Bruzual & Charlot (2003; hereafter BC03) instantaneous burst model with solar metallicity and an age of 5 Gyr was used as our spectral template. We then produced thirteen redshifted templates between  $z = 0.4$  and  $z = 1.0$ , stepping in intervals of 0.05. Convolution of these redshifted templates through the nine filters of SDSS/UKIDSS photometry (Hewett et al. 2006) then generated magnitudes and therefore colors. Using the Structured Query Language (SQL) for data in the Wide Field Camera Science Archive (WSA) on UKIRT, we searched the combined UKIDSS/SDSS database for objects (1) that have colors matching our template at a given redshift, (2) that are compact enough such that  $-0.1 < \text{UKIDSS } K(\text{Petrosian}) - K(1'' \text{ aperture}) < 0.3$ , and (3) that are at least one magnitude brighter than  $L^*$ <sup>4</sup> for elliptical galaxies in  $H$  band at that redshift. Separate SQL searches were made at the thirteen redshifts between 0.4 to 1.0. Based on UKIDSS  $J_1$ -band images of objects that passed the SQL, we selected our candidates for follow-up observations by choosing compact ones whose surface brightness profiles resemble nearby stars in the same field.

Our candidate selection procedure was not able to distin-

guish compact galaxies from stars and QSOs. We therefore needed to examine these candidates with deep and high-resolution images to select objects for spectroscopic follow-up. Based on our Keck and Subaru observations, we removed all the stars and QSOs, as well as galaxies that have effective radii  $R_e > 3 \text{ kpc}$ . Our final sample in this paper comprises 22 galaxies with both imaging and spectroscopic data available, allowing the determination of their redshifts and effective radii.

### 2.2. Imaging

The galaxies in sample 1 were imaged in  $H$  or  $K'$  band on various nights from 2009 to 2011 with the NIRC2 camera and the laser-guide-star adaptive optics system (LGSAO; Wizinowich et al. 2006) on the Keck II telescope. These fifteen fields were all selected to have at least one good signal-to-noise star in the field of view for determining the point-spread function (PSF) of the image. The exposure times ranged from  $60 \text{ s} \times 5$  to  $180 \text{ s} \times 9$ , and the image scale is  $0''.04 \text{ pixel}^{-1}$ . For the galaxies in sample 2, we obtained  $I$ -band images with the imaging mode of the Faint Object Camera and Spectrograph (FOCAS; Kashikawa et al. 2002) on the Subaru telescope on March 4 and 5, 2013. The exposure times range from  $60 \text{ s} \times 5$  to  $60 \text{ s} \times 15$ , and the image scale is  $\sim 0''.1 \text{ pixel}^{-1}$ . We reduced our data with IRAF following standard procedures including bias subtraction and flat-fielding. Individual dithered images were then registered and combined with the drizzle algorithm (Fruchter & Hook 2002).

### 2.3. Spectroscopy

We carried out ground-based spectroscopy for fourteen galaxies in sample 1 with the Low-Resolution Imaging Spectrograph (LRIS; Oke et al. 1995) on the Keck I telescope and one galaxy (SDSSJ081053) with the Echellette Spectrograph and Imager (ESI; Sheinis et al. 2002) on the Keck II telescope. The LRIS spectra were obtained with the 600 line  $\text{mm}^{-1}$  grating (FWHM resolution:  $4.7 \text{ \AA}$ ) blazed at 5000 or 7500  $\text{\AA}$  on the red side of the spectrograph. The ESI spectrum was taken with the echellette mode using the 175 line  $\text{mm}^{-1}$  grating (FWHM resolution:  $1.3 \text{ \AA}$ ). For the objects in sample 2, we took their spectra with the spectroscopic mode of FOCAS on the Subaru telescope using the VPH850 grism and SO58 filter (FWHM resolution:  $11 \text{ \AA}$ ). Standard data reduction procedures including bias subtraction, flat-fielding, sky subtraction, wavelength and flux calibrations were performed with IRAF to extract the 1D spectra. Spectroscopic redshifts of galaxies are determined by cross-correlation between reduced spectra and spectral templates in the IDL routine SPECPRO developed by Masters & Capak (2011). The spectra of SDSSJ012942, SDSSJ081053 and SDSSJ235219 do not have well-calibrated continua due to calibration problems, but the detection of absorption lines and the 4000  $\text{\AA}$  break still allows precise determination of redshifts. In Table 1, we summarize our imaging and spectroscopic observations.

## 3. DATA ANALYSIS AND RESULTS

### 3.1. Morphologies

From our Keck/NIRC2 and Subaru/FOCAS imaging, we explored the structural parameters of our objects with GALFIT (Peng et al. 2002, 2010), a routine for determining models of the two-dimensional galaxy profile by minimizing the  $\chi^2$  residuals. For each AO image, we determined the PSF

<sup>4</sup> We use the term “ $L^*$  galaxy” to mean a galaxy at a given redshift that will, through passive evolution alone, end up as an  $L^*$  galaxy at the present epoch (Huang et al. 2003); i.e., we do not attempt to take into account any evolution of the shape of the luminosity function. Operationally, we take a present-day early-type  $L^*$  galaxy represented by a Bruzual & Charlot (2003) model formed at  $z = 9$  and follow the SED back in redshift, determining expected magnitudes at each interval in  $z$ .

profile from the nearest unsaturated star, usually within  $25''$  of the galaxy. We have done tests in globular cluster fields and have found that on most nights the PSF does not change significantly for our purposes over this distance. In any case, in agreement with Carrasco et al. (2010), we have found that the basic galaxy structural parameters are fairly robust against uncertainties in the PSF core width. For the FOCAS imaging, the PSF is essentially invariant over a large field, so a suitable PSF star can always be found. Using the PSFs we determined, we first fitted single-Sérsic models (Sérsic 1968) to the galaxy images, as shown in the first rows of all the objects in Figure A1 and A2. One exception was for SDSSJ011004, where there is a companion very close to the galaxy, so we simply included this object in the fit using another single-Sérsic model. These fits resulted in circularized effective radii of  $R_e < 3$  kpc for all the objects.

We chose the best GALFIT results by both visual inspection of the residuals and the reduced  $\chi^2$  of the fits. For eight galaxies, the single-component fits left significant systematic residuals. Three of these eight galaxies have unusual Sérsic indices of  $n > 6$ , which is a clear indication that double-Sérsic models are needed. We therefore performed two-component fits for these eight objects, as shown in the second rows of eight objects in Figure A1, leading to better residuals and reduced  $\chi^2$ . However, two of these galaxies, SDSSJ014355 and SDSSJ115836, both turned out to have best-fit Sérsic indices of  $n \sim 4$  and  $n < 0.5$  for their two components. Since  $n < 0.5$  implies an unphysical central dip in the three-dimensional stellar distribution, we forced  $n = 0.5$  for their second components and ran the fits again. This resulted in  $n = 4.09$  and  $n = 3.90$  for their first components, which remain close to the  $r^{1/4}$  law. We also tried adding a second component to the fits for all the other galaxies. Nevertheless, the reduced  $\chi^2$  either remained roughly unchanged or became smaller but further away from unity (a sign of “over-fitting”), suggesting that single-Sérsic models are sufficient.

Spectroscopic redshifts determined from the reduced galaxy spectra (Table 2) allow us to convert the effective radii in unit of pixels to physical scales based on the assumed cosmology in this paper. Table 2 and Table 3 summarize the best-fit parameters of single-Sérsic and double-Sérsic models, respectively. In the rest of this paper, we will use the circularized effective radius as a proxy for galaxy size. The practice of using the circularized effective radius has traditionally been used to account for the uncertainty of the projection of ellipsicals and spheroids due to their triaxiality.

### 3.2. Spectral Energy Distributions and Stellar Populations

To constrain the stellar populations of the galaxies, we used FAST (Kriek et al. 2009) to fit BC03 models simultaneously to SDSS/UKIDSS magnitudes and flux-calibrated spectra for most of our objects. For four galaxies, we only fitted models to SDSS/UKIDSS magnitudes due to low S/N or flux calibration problems of the spectra. We used BC03 models with exponentially declining star formation rates, all with Chabrier (2003) IMF, Calzetti reddening law (Calzetti et al. 2000), and metallicities  $[Z/H]$  of  $-0.4$ ,  $0.0$  and  $0.4$ . All the magnitudes and spectra were corrected for galactic extinction according to NASA/IPAC Extragalactic Database (NED), and redshifts were fixed at the spectroscopic redshifts in the fits. The best-fit model parameters as well as the corresponding mean ages and stellar masses of galaxies are tabulated in Table 4. Notice that the “age” of a BC03 model with exponentially declining star formation rate represents the age since the onset of star

formation. On the other hand, the mean age of the stellar population is the age since one  $\tau$  ( $e$ -folding timescale for the star formation rate) after the onset of star formation.

### 3.3. Full-Spectrum Fitting

#### 3.3.1. Stellar Populations

It is well-known that an age-metallicity degeneracy exists in the determination of stellar populations from broadband photometry. Given that one old and low-metallicity spectrum may have the same shape, and therefore same broadband colors, as a young and high-metallicity spectrum, breaking this degeneracy relies on the differences in detail at absorption lines between similar spectra. To do this, the full-spectrum fitting method is recently becoming a popular alternative to using line-strength indices, thanks to the availability of high-quality spectral-synthesis models.

We therefore used the Penalized Pixel-Fitting method (pPXF) by Cappellari & Emsellem (2004) to constrain the stellar populations from ten spectra that have high S/N and well-calibrated continua. For each galaxy, a grid of BC03 instantaneous burst models were used with three metallicities and ages stepping in intervals of  $\sim 0.25$  Gyr from 0.005 Gyr to the maximum age younger than the age of universe at the galaxy redshift. We shifted the spectra to the rest frame, corrected for galactic extinction, logarithmically rebinned the wavelength grid, and masked bad pixels. Model templates were broadened with a Gaussian to match the instrumental resolution of the de-redshifted spectra. The best-fit solution provided by pPXF is a distribution of the mass fraction in different ages and metallicity intervals, i.e., a linear combination of different BC03 models. This allows us to obtain probabilities of star formation at different cosmic time instead of a single age for each of the galaxies we analyzed. Running pPXF involves choosing a regularization parameter that affects the smoothness of the solutions. Here we assume that the initial starbursts of these galaxies were intense and rather brief since strong dissipation must have been involved to account for their compactness. We chose regularization parameters that led to fairly narrow distributions for the major star-formation periods, rather than the smoothest possible distribution consistent with the spectra. However, it should be noted that our choice is an assumption instead of a result.

Figure A3 shows the fits and the corresponding distributions of star formation over cosmic time. We calculated the mean mass-weighted as well as mean luminosity-weighted ages and metallicities of these distributions, as shown in Table 5. The age of a galaxy determined by FAST should be considered as a luminosity-weighted average result. Our mean luminosity-weighted ages based on the full-spectrum fits roughly agree with the mean ages given by FAST (column 4 of Table 4). We can also calculate the stellar mass of a galaxy from the optimized linear combination of BC03 models. In order to account for the flux loss of the slit, we scaled our best-fit model to match the broadband photometry. The derived masses are listed in column 7 of Table 5.

The uncertainties in the derived quantities are difficult to estimate, since it is likely that they will be dominated by systematic effects that are largely unknown, such as the accuracy of the models. In general, variations within an allowed range from the minimum  $\chi^2$  value, governed by the regularization parameter, typically change the width (and sometimes slightly the ages) of the star-forming episodes, without changing the stellar mass by very much. In any case, at present, it is

impractical to attempt to derive the random uncertainties for population analyses via automated Monte Carlo simulations (such as we are able to use for measuring the velocity dispersions, as described in Section 3.3.2) because of the required tuning of the spectral noise level and the regularization parameter. Thus, the models and the associated derived parameters can only be taken as indicative. To some extent (again subject to uncertainty of the models), confidence in the general accuracy of the solution can be judged by the agreement of different approaches, such as the degree of agreement of the luminosity-weighted ages from pPXF with the ages given by FAST, as mentioned above.

We have performed some additional tests for the case of SDSSJ014355, which, as discussed in Section 4.4, is the best candidate from the current samples of a mostly intact survivor from the high-redshift compact galaxy population. We tried running pPXF on this spectrum while constraining the stellar metallicities to single values of  $[Z/H] = -0.4, 0.0$  and  $0.4$ . Although our original fit, as well as these single-metallicity fits, depend on both the continuum shape and sharp absorption features, when we eliminate the effect of the continuum by subtracting a low-order fit to the residuals (observed spectrum minus model), testing only the fit to absorption lines and breaks, the residual noise is significantly lower in our original multi-metallicity fit than in any of the others. Because of the dominance of a low-metallicity population in the best fit, this object is useful for testing the influence of the well-known age-metallicity degeneracy. The  $[Z/H] = -0.4$  model, as expected, is dominated by a maximally old population. The solar-metallicity model is strongly dominated by a starburst peaking at about 6.3 Gyr, or at a redshift of  $\sim 2.9$ . Only the super-solar model has a substantial fraction of the stellar mass formed at low redshifts, with about half with an age of  $\sim 3$  Gyr, and most of the other half with an age of  $\sim 8$  Gyr (formed at  $z \sim 9.3$ ). However, all of these single-metallicity models are unrealistic in terms of chemical evolution in galaxies and they are significantly worse fits to the observed spectrum.

### 3.3.2. Velocity Dispersions and Dynamical Masses

We also used the pPXF code to calculate the velocity dispersions of these eleven galaxies. In order to estimate the errors, we followed Toft et al. (2012) and ran Monte Carlo simulations in the following way. We subtracted the best-fit model from the spectrum, and the residuals were randomly rearranged in wavelength space and added to the best-fit model to create 100 mock spectra. This led to a distribution of measured velocity dispersions, and the standard deviation is taken as the  $1\text{-}\sigma$  error.

Combining the measurements of effective radii and velocity dispersions, we were able to estimate dynamical masses and compare the values with the stellar masses inferred from the stellar populations. For spheroids, the equation of the dynamical mass is

$$M_{\text{dyn}} = \beta R_e \sigma^2 / G, \quad (1)$$

where  $\beta$  is a parameter that depends mainly on the structure of the galaxy. Cappellari et al. (2006) found that  $\beta = 5.0 \pm 0.1$  accurately reproduces galaxy dynamical masses for local ellipticals, and this value is commonly used in the literature. In column 8 and 9 of Table 5, we tabulate the velocity dispersions and the dynamical masses assuming  $\beta = 5$ . In this calculation, we adopted equation 1 of Cappellari et al. (2006) to correct the measured velocity dispersion  $\sigma$  to  $\sigma_e$ , which

would be the velocity dispersion measured within  $R_e$ . However, we can see clear discrepancies between the dynamical and stellar masses estimates. In agreement with what has been found in several recent studies for compact massive galaxies (e.g., Stockton et al. 2010; Martinez-Manso et al. 2011; Ferré-Mateu et al. 2012), the stellar masses of most galaxies are unphysically larger than their dynamical masses. This indicates that we cannot assume homology between our galaxies and local ellipticals studied by Cappellari et al. (2006), and the assumption that  $\beta = 5$  may not be correct. This discrepancy caused by different galaxy structures is recently reinforced by Peralta de Arriba et al. (2014), who find an empirical relation between  $\beta$  ( $K$  in their paper) and the compactness of galaxies. In the last column of Table 5, we tabulate the dynamical masses with the correction in Peralta de Arriba et al. (2014). Most of these values are about two times the corresponding stellar masses; the median value of dynamical-to-stellar-mass ratios is 1.84.

## 4. DISCUSSION AND CONCLUSION

### 4.1. Current Star-Formation Rates

Our selection procedure was designed to eliminate objects with significant current star formation, and our spectra indicate that this goal has been achieved. None of our spectra shown here have detectible  $[\text{O II}] \lambda 3727$  emission (for SDSS J105745, we do not observe this spectral region). In order to estimate rough upper limits to the star formation rates, we consider a typical galaxy with  $z = 0.6$ ,  $r = 21.6$ , for which the spectrum gives a  $S/N = 12$  at  $4200 \text{ \AA}$ . We model a  $2\sigma$  line at the position of  $[\text{O II}] \lambda 3727$ , which gives a flux of  $2 \times 10^{-17} \text{ ergs s}^{-1} \text{ cm}^{-2}$ . Using the relation between  $[\text{O II}]$  flux and star-formation rate (SFR) given by Kewley et al. (2004; eq. 4), we obtain an upper limit to the SFR of  $0.2 M_{\odot} \text{ yr}^{-1}$  for this case. We have only one object at a substantially higher redshift, but for that case we also have about twice the  $S/N$  that we have assumed. Even taking into account various plausible uncertainties, we can place a conservative SFR upper limit of the galaxies in our sample of  $< 1 M_{\odot} \text{ yr}^{-1}$ .

### 4.2. Mass-Size Relations and Ages

In Figure 1, we plot the mass-size relations of our galaxies and compare them with SDSS galaxies at  $0.05 < z < 0.07$  from Franx et al. (2008), the compact quiescent galaxies found at  $z > 2$  from van Dokkum et al. (2008), and the five  $z \sim 0.5$  galaxies from Stockton et al. (2014). In this plot, most of our galaxies locate in the area between SDSS sample and the extremely compact galaxies from the other two papers; some of them are indistinguishable from the SDSS sample. This implies that most of our galaxies are not survivors of high-redshift population of compact quiescent galaxies. Our constraint on stellar populations with FAST suggests that half of the galaxies in our sample have mean ages  $\lesssim 2$  Gyr, which lines up with some recent studies that found young ages for local compact quiescent galaxies (e.g., Trujillo et al. 2009; Ferré-Mateu et al. 2012).

### 4.3. Disk-like Galaxies

Many of our galaxies show signs of disks based on the morphological analysis. We classify the eight galaxies fitted by two-component models (Table 3) as disk-like galaxies because each of their best-fit models is either a superposition of two components with  $n < 2.5$ , or a compact core with  $n > 2.5$  plus an extended component with  $n < 2.5$ . For six out of

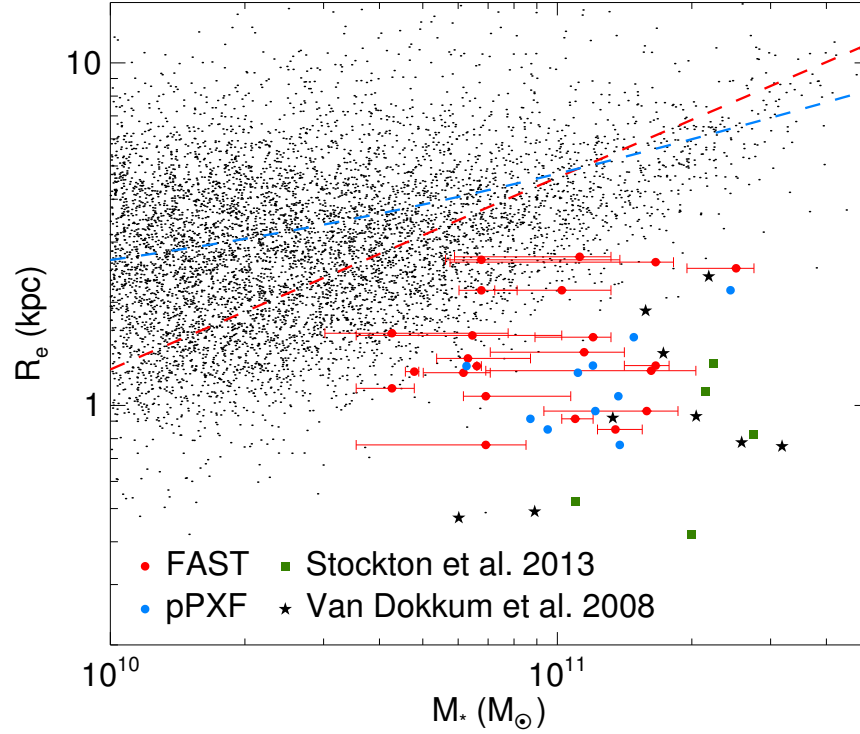


FIG. 1.— Relations between the stellar masses determined by FAST (red; all the 22 galaxies) or pPXF (blue; 10 galaxies) and the sizes for our sample. Notice that we omit the errors of the circularized effective radii since their error bars are smaller than or comparable to the sizes of red and blue data points in this plot. Small dots are SDSS galaxies at  $0.05 < z < 0.07$  from Franx et al. (2008). Red and blue dashed lines indicate the mass-size relations for local early-type and late-type galaxies, respectively, from Shen et al. (2003). Green squares are the five galaxies from Stockton et al. (2014). Black stars are the  $z > 2$  compact quiescent galaxies from van Dokkum et al. (2008), for which we omit the errors.

these eight galaxies (the exception being SDSSJ011004 and SDSSJ115836), the axis ratio  $b/a$  of the more extended component is much lower than the axis ratios of the other component and the single-Sérsic model. As a result, these six objects have significant residuals along their major axes in one-component fits as shown in Figure A1. For SDSSJ115836, the residual in the one-component fit has a ring-like distribution, and both components in the double-Sérsic model have  $b/a > 0.5$ . We believe the morphology of this object is similar to the above six galaxies except that it is relatively face-on. In addition, there are four galaxies (SDSSJ115027, SDSSJ124257, SDSSJ135342 and SDSSJ164916) described by single-Sérsic models with  $n < 2.5$ . We therefore classify these four objects as another four disk-like galaxies.

In total, we have 12 out of 22 (55%) galaxies that are disk-like. We can compare this fraction with the result of Buitrago et al. (2013), who calculated the fractions of massive galaxies showing disk-like surface brightness profiles ( $n < 2.5$ ) and spheroid-like ones ( $n > 2.5$ ) as a function of redshift between  $z = 0$  and  $z = 3$ . The median redshift of our sample is  $\sim 0.6$ , which corresponds to a disk-like fraction of  $\sim 25\%$  according to Figure 7 in Buitrago et al. (2013). Our sample of compact quiescent galaxies has a higher disk-like fraction than do massive galaxies generally at the same redshift range. This high disk-like fraction could be a result of young ages we found in our sample. Besides SDSSJ014355, SDSSJ115836, SDSSJ135342 and SDSSJ235219, two-thirds of our disk-like galaxies have fairly young ages, or at least have significant star formation in the past 2 Gyr as indicated by our full-spectrum fits (SDSSJ084223 and SDSSJ155037).

Our result lines up with previous studies (Stockton et al. 2004, 2008; van Dokkum et al. 2008; McGrath et al. 2008; van der Wel et al. 2011; Chang et al. 2013a,b; McLure et al. 2013) which found that massive quiescent galaxies at high redshifts often have disk-like morphologies.

Some simulations have shown that gas-rich mergers can produce disk remnants (e.g., Hopkins et al. 2009b; Puech et al. 2012). However, what these simulations produced are large thin disks, which do not resemble the compact galaxies discovered at high redshifts or in this work. This is because a significant amount of gas needs to be driven to large radii, where it does not feel strong torques from the merger and retains its angular momentum to form disks. If these galaxies indeed have rotating and disk-like structures, their formation mechanism should involve extreme dissipation to have gas settle onto a disk before converting into stars, but it also has to be rapid enough to account for their compactness.

Another possibility is that these galaxies are actually prolate, with radial orbits mostly aligned with the long axis. As suggested by Stockton et al. (2014), such a morphology could probably explain the discrepancy between the calculated stellar mass and the dynamical mass estimated from the relation that works well for local elliptical galaxies. Also, the fact that prolate galaxies do not exist locally is an indication that galaxy formation mechanisms may be different at different cosmic times. Further work, including high-spatial-resolution spectroscopy, is needed to examine whether or not these compact galaxies are rotationally supported. Based on integral field spectroscopic measurement of  $H\alpha$  emission lines, Buitrago et al. (2014) have found evidence of rotational

support for 10 massive galaxies at  $z \sim 1.4$  and confirmed that half of them are rotating disks. Although their sample is not selected to be compact and quiescent, as ours is (only having absorption-line spectra), this work does support the idea that disks are common among massive galaxies at high redshifts.

#### 4.4. Old Galaxies

Our pPXF fits show that SDSSJ014355, SDSSJ101009, SDSSJ115836 and SDSSJ105745 have more than 90% (by mass) of their stellar populations formed at  $z > 2$ . The best-fit BC03 model with exponentially declining star formation rate from FAST for SDSSJ134412 also suggests formation of  $\sim 80\%$  of the stellar mass at  $z > 2$ . This indicates that these galaxies are possibly slightly modified survivors of the high-redshift population of massive compact quiescent galaxies. On the other hand, the old ages of SDSSJ235219, SDSSJ091515 and SDSSJ135342 determined by FAST have large uncertainties, so deeper spectroscopic data for full-spectrum fits are needed to better constrain their stellar population properties.

van Dokkum et al. (2010) suggest that the mass growth of massive galaxies is due to a gradual buildup of outer envelopes over time around the compact cores observed at high redshifts. Parameterizing the surface brightness profiles of massive galaxies, they found that both the effective radius and Sérsic index increase towards low redshifts. Based on this scenario of inside-out growth of massive galaxies, old quiescent galaxies in the local universe are expected to have high Sérsic indices and not be disk-like. The Sérsic indices of SDSSJ101009, SDSSJ134412 and SDSSJ105745 are consistent with this scenario. Therefore, these three galaxies had likely been modified and do not show their original structural properties. The absence of stellar disks of these galaxies may be a result of major mergers or a sequence of many minor mergers (Bournaud et al. 2007).

SDSSJ014355 and SDSSJ115836, in contrast, have different morphologies; they are classified as disk-like galaxies that are fitted by two-component models (Section 4.3). The pPXF model for SDSSJ014355 has  $\sim 3\%$  of  $\sim 500$ -Myr-old star formation being added to a dominant population formed at  $z > 6$ , and it has a much smaller size than the other four old galaxies we discuss here ( $R_e = 0.77$  kpc). The pPXF model for SDSSJ115836 also indicates  $\sim 3\%$  of  $\sim 1$ -Gyr-old star formation and a dominant population formed at  $z > 3$ . It is possible that these two galaxies are nearly unaltered relics from the high-redshift massive compact galaxy population. Especially, the extreme compactness of SDSSJ014355 might be a result of formation in dense environment at the very early universe. If these galaxies were indeed disk-like survivors from high redshift, it would again support the idea that massive quiescent galaxies at high redshifts are often disk-like. However, the GALFIT modes of these two objects both consist of cores with  $n \sim 4$  and fainter, extended disks. Therefore, it is also possible that the extended components are caused by recent gas accretion and star formation added onto the old compact cores. In any case, it would be very useful to perform spatially resolved spectroscopy or multi-wavelength imaging to compare the ages or colors of the cores and the outer envelopes, determining whether such structures are intrinsic to the formation process or modified by more recent star formation.

## 5. SUMMARY

Our search for luminous compact quiescent galaxies at  $0.4 < z < 1.0$  has returned a sample of objects that allows detailed studies with imaging and spectroscopic follow-up. Although this search is far from being complete and unbiased, it does offer a way for us to infer the formation of massive galaxies at  $z > 2$  and to study their structural change at lower redshifts. Our result again suggests that unmodified relics from the population of high-redshift compact quiescent galaxies are indeed rare; most of the massive galaxies we found actually formed at  $z < 2$ , where the density of universe was lower than high redshifts. These young galaxies are less compact than those found at  $z > 2$  in the literature. Interestingly, several of these young objects appear to be disk-like or possibly prolate. If these galaxies were to be confirmed to be disks, their formation mechanism should involve extreme dissipation to have gas settle onto a disk before converting into stars. The models for forming massive compact galaxies through major mergers would need more tests in order to account for both compact and disk-like structures. On the other hand, if these galaxies were to be confirmed to be prolate, it would indicate that galaxy formation mechanisms have evolved over cosmic time. More studies need to be done to determine the actual morphologies of these galaxies.

Three out of five of the galaxies that formed more than 80% of their masses at  $z > 2$  based on our analysis have morphologies similar to the local ellipticals. Building up of these galaxies by mergers or accretion might have already happened and therefore altered their structures. In contrast, SDSSJ014355 and SDSSJ115836 are likely nearly unmodified disk-like galaxies that are worth more future work. Recently, Trujillo et al. (2014) has discovered that NGC1277, a lenticular galaxy at a distance of only  $\sim 73$  Mpc, is an unmodified relic from the high-redshift massive compact galaxy population. One interesting characteristic of NGC1277 is its low Sérsic index of  $n = 2.2$ , again indicating a disk-like structure. It would be of great interest to obtain detailed IFU observations to examine the stellar dynamics of this galaxy. This discovery also raises some hope of finding more such type of galaxies in the local universe where we can perform very detailed analysis.

We thank the anonymous referee for a careful and thoughtful reading of the original version of this paper and for offering numerous suggestions to improve both its substance and presentation. We also thank Allison Man for helpful discussions. This research has been partially supported by NSF grant AST-0807900. The UKIDSS project is defined in Lawrence et al. (2007). UKIDSS uses the UKIRT Wide Field Camera (WFCAM; Casali et al. 2007) and a photometric system described in Hewett et al. (2006). The pipeline processing and science archive are described in Hambly et al. (2008). Funding for the SDSS has been provided by the Alfred P. Sloan Foundation, the Participating Institutions, the National Science Foundation, the U.S. Department of Energy, the National Aeronautics and Space Administration, the Japanese Monbukagakusho, the Max Planck Society, and the Higher Education Funding Council for England. The SDSS website is found at <http://www.sdss.org/>.

*Facilities:* Keck:I (LRIS), Keck:II (LGSAO/NIRC2/ESI), Sloan (SDSS), Subaru (FOCAS), UKIRT (UKIDSS)

TABLE 1  
SUMMARY OF OBSERVATIONS.

Object Name	SDSS		Imaging				Spectroscopy		
	$r^a$	Date (UT)	Exposure (s)	Filter	$\text{mag}^b$	$1\sigma^c$	Date (UT)	Exposure (s)	S/N <sup>d</sup>
SDSS J011004.73+140933.0	21.40	20090915	1080	<i>H</i>	18.81	23.66	20090822	3600	23.6
SDSS J012942.10+132420.8	21.35	20110826	300	<i>H</i>	19.00	23.48	20100816	1200	11.6
SDSS J014355.21+133451.4	20.93	20110826	300	<i>H</i>	18.83	23.48	20100906	3600	24.9
SDSS J081053.07+230443.7	21.36	20120328	1080	<i>K'</i>	18.86	24.29	20120314(ESI)	900	10.8
SDSS J084223.93+050223.4	20.72	20110426	1080	<i>H</i>	18.72	24.30	20110426	2400	19.0
SDSS J084616.69+052833.6	20.45	20110426	1080	<i>H</i>	18.61	24.09	20110426	2400	19.5
SDSS J101009.25+062324.8	21.22	20110426	1620	<i>H</i>	18.83	25.28	20110426	3600	13.5
SDSS J115836.93+021535.1	21.46	20100406	1080	<i>H</i>	19.03	24.31	20100408	3420	11.3
SDSS J121954.26+003025.2	20.21	20100406	960	<i>H</i>	18.54	24.24	20100320	600	6.0
SDSS J123106.94+053347.6	20.93	20110426	1440	<i>H</i>	18.73	24.19	20110426	3600	19.9
SDSS J124257.04+102400.7	20.73	20110426	1080	<i>H</i>	18.61	23.78	20110426	4800	23.6
SDSS J134412.30+010906.6	20.56	20110426	1620	<i>H</i>	18.48	23.86	20110426	3600	9.3
SDSS J155037.84+024746.5	21.04	20100406	1080	<i>H</i>	18.74	24.67	20100320	3600	15.5
SDSS J164916.12+294309.0	20.54	20100406	840	<i>H</i>	18.79	23.73	20100408	600	10.5
SDSS J235219.98−004855.7	21.08	20090915	840	<i>H</i>	18.66	23.98	20090822	1200	5.2
SDSS J091515.64+055256.9	23.76	20130304	300	<i>I</i>	21.62	26.32	20130304	600	3.0
SDSS J104224.46+022225.0	21.85	20130305	300	<i>I</i>	20.74	25.99	20130305	900	10.2
SDSS J104630.88−010759.0	21.60	20130304	300	<i>I</i>	20.36	26.08	20130304	600	6.0
SDSS J105745.85−005818.6	21.53	20130305	600	<i>I</i>	20.41	26.15	20130304&0305	4200	24.9
SDSS J115027.99+025118.1	21.54	20130304	300	<i>I</i>	20.58	26.29	20130304	600	5.2
SDSS J132953.78+295140.0	22.89	20130304	300	<i>I</i>	21.44	26.33	20130304	900	4.8
SDSS J135342.06+262157.1	21.56	20130304	300	<i>I</i>	20.31	26.22	20130304	900	5.3

NOTE. — For the upper block (sample 1), all the objects were imaged with Keck II/NIRC2, and spectra were taken with Keck I/LRIS except for SDSS J081053.07+230443.7, which was taken with Keck II/ESI. All the objects in the lower block (sample 2) were observed with Subaru/FOCAS for both imaging and spectroscopic modes.

<sup>a</sup>SDSS  $r$ -band magnitude

<sup>b</sup>magnitude of the object in the corresponding filter

<sup>c</sup> $1\sigma$  limiting magnitude of each image. A  $2''$  diameter aperture and a  $5''$  diameter aperture are used to calculate the magnitudes for NIRC2 and FOCAS images, respectively.

<sup>d</sup>Median value of the signal-to-noise ratio per pixel at the red side of 4000

Å break.

## REFERENCES

- Baldry, I. K., Glazebrook, K., Brinkmann, J., et al. 2004, *ApJ*, 600, 681  
 Bezanson, R., van Dokkum, P. G., Tal, T., et al. 2009, *ApJ*, 697, 1290  
 Bouchaud, F., Jog, C. J., & Combes, F. 2007, *A&A*, 476, 1179  
 Bruce, V. A., Dunlop, J. S., Cirasuolo, M., et al. 2012, *MNRAS*, 427, 1666  
 Bruzual, G., & Charlot, S. 2003, *MNRAS*, 344, 1000  
 Buitrago, F., Conselice, C. J., Epinat, B., et al. 2014, *MNRAS*, 439, 1494  
 Buitrago, F., Trujillo, I., Conselice, C. J., et al. 2008, *ApJ*, 687, L61  
 Buitrago, F., Trujillo, I., Conselice, C. J., & Häußler, B. 2013, *MNRAS*, 428, 1460  
 Calzetti, D., Armus, L., Bohlin, R. C., et al. 2000, *ApJ*, 533, 682  
 Cappellari, M., & Emsellem, E. 2004, *PASP*, 116, 138  
 Cappellari, M., Bacon, R., Bureau, M., et al. 2006, *MNRAS*, 366, 1126  
 Carrasco, E. R., Conselice, C. J., & Trujillo, I. 2010, *MNRAS*, 405, 2253  
 Casali, M., Adamson, A., Alves de Oliveira, C., et al. 2007, *A&A*, 467, 777  
 Chabrier, G. 2003, *PASP*, 115, 763  
 Chang, Y.-Y., van der Wel, A., Rix, H.-W., et al. 2013a, *ApJ*, 762, 83  
 —. 2013b, *ApJ*, 773, 149  
 Daddi, E., Renzini, A., Pirzkal, N., et al. 2005, *ApJ*, 626, 680  
 Damjanov, I., Chilingarian, I., Hwang, H. S., & Geller, M. J. 2013, *ApJ*, 775, L48  
 Damjanov, I., McCarthy, P. J., Abraham, R. G., et al. 2009, *ApJ*, 695, 101  
 Dekel, A., Sari, R., & Ceverino, D. 2009, *ApJ*, 703, 785  
 Fan, L., Lapi, A., Bressan, A., et al. 2010, *ApJ*, 718, 1460  
 Fan, L., Lapi, A., De Zotti, G., & Danese, L. 2008, *ApJ*, 689, L101  
 Ferré-Mateu, A., Vazdekis, A., Trujillo, I., et al. 2012, *MNRAS*, 423, 632  
 Franx, M., van Dokkum, P. G., Schreiber, N. M. F., et al. 2008, *ApJ*, 688, 770  
 Fruchter, A. S., & Hook, R. N. 2002, *PASP*, 114, 144  
 Hambly, N. C., Collins, R. S., Cross, N. J. G., et al. 2008, *MNRAS*, 384, 637  
 Hewett, P. C., Warren, S. J., Leggett, S. K., & Hodgkin, S. T. 2006, *MNRAS*, 367, 454  
 Hopkins, P. F., Bundy, K., Murray, N., et al. 2009a, *MNRAS*, 398, 898  
 Hopkins, P. F., Cox, T. J., Younger, J. D., & Hernquist, L. 2009b, *ApJ*, 691, 1168  
 Hopkins, P. F., Hernquist, L., Cox, T. J., et al. 2006, *ApJS*, 163, 1  
 Huang, J.-S., Glazebrook, K., Cowie, L. L., & Tinney, C. 2003, *ApJ*, 584, 203  
 Kashikawa, N., Aoki, K., Asai, R., et al. 2002, *PASJ*, 54, 819  
 Kewley, L. J., Geller, M. J., & Jansen, R. A. 2004, *AJ*, 127, 2002  
 Khochfar, S., & Silk, J. 2006, *ApJ*, 648, L21  
 Kriek, M., van Dokkum, P. G., Labbé, I., et al. 2009, *ApJ*, 700, 221  
 Lawrence, A., Warren, S. J., Almaini, O., et al. 2007, *MNRAS*, 379, 1599  
 Longhetti, M., & Saracco, P. 2009, *MNRAS*, 394, 774  
 López-Sanjuan, C., Balcells, M., Pérez-González, P. G., et al. 2010, *ApJ*, 710, 1170  
 Martínez-Manso, J., Guzmán, R., Barro, G., et al. 2011, *ApJ*, 738, L22  
 Masters, D., & Capak, P. 2011, *PASP*, 123, 638  
 McGrath, E. J., Stockton, A., Canalizo, G., Iye, M., & Maihara, T. 2008, *ApJ*, 682, 303  
 McLure, R. J., Pearce, H. J., Dunlop, J. S., et al. 2013, *MNRAS*, 428, 1088  
 Naab, T., Johansson, P. H., & Ostriker, J. P. 2009, *ApJ*, 699, L178  
 Oke, J. B., Cohen, J. G., Carr, M., et al. 1995, *PASP*, 107, 375  
 Peng, C. Y., Ho, L. C., Impey, C. D., & Rix, H.-W. 2002, *AJ*, 124, 266  
 —. 2010, *AJ*, 139, 2097  
 Peralta de Arriba, L., Balcells, M., Falcón-Barroso, J., & Trujillo, I. 2014, *MNRAS*, 440, 1634  
 Poggianti, B. M., Calvi, R., Bindoni, D., et al. 2013, *ApJ*, 762, 77  
 Puech, M., Hammer, F., Hopkins, P. F., et al. 2012, *ApJ*, 753, 128  
 Quilis, V., & Trujillo, I. 2013, *ApJ*, 773, L8  
 Sersic, J. L. 1968, *Atlas de galaxias australes*  
 Sheinis, A. I., Bolte, M., Epps, H. W., et al. 2002, *PASP*, 114, 851  
 Shen, S., Mo, H. J., White, S. D. M., et al. 2003, *MNRAS*, 343, 978  
 Shih, H.-Y., & Stockton, A. 2011, *ApJ*, 733, 45

TABLE 2  
SPECTROSCOPIC REDSHIFTS AND PARAMETERS OF SINGLE-SÉRSIC MODELS.

Object Name	$z_{spec}$	$R_e$ (kpc)	$n$	$b/a$
SDSS J011004.73+140933.0	0.801	$0.91 \pm 0.00$	$2.92 \pm 0.01$	0.37
SDSS J012942.10+132420.8	0.582	$1.12 \pm 0.01$	$3.05 \pm 0.03$	0.56
SDSS J014355.21+133451.4	0.487	$0.77 \pm 0.01$	$3.77 \pm 0.04$	0.29
SDSS J081053.07+230443.7	0.636	$1.37 \pm 0.01$	$6.51 \pm 0.05$	0.27
SDSS J084223.93+050223.4	0.557	$1.25 \pm 0.00$	$1.92 \pm 0.01$	0.26
SDSS J084616.69+052833.6	0.589	$1.06 \pm 0.01$	$3.81 \pm 0.05$	0.91
SDSS J101009.25+062324.8	0.542	$1.31 \pm 0.02$	$5.12 \pm 0.05$	0.45
SDSS J115836.93+021535.1	0.587	$2.17 \pm 0.04$	$7.63 \pm 0.08$	0.56
SDSS J121954.26+003025.2	0.412	$1.60 \pm 0.02$	$5.87 \pm 0.05$	0.34
SDSS J123106.94+053347.6	0.642	$0.96 \pm 0.00$	$2.98 \pm 0.02$	0.45
SDSS J124257.04+102400.7	0.680	$0.85 \pm 0.00$	$2.11 \pm 0.01$	0.26
SDSS J134412.30+010906.6	0.532	$2.51 \pm 0.02$	$4.07 \pm 0.02$	0.76
SDSS J155037.84+024746.5	0.553	$1.30 \pm 0.01$	$3.31 \pm 0.01$	0.45
SDSS J164916.12+294309.0	0.531	$1.26 \pm 0.01$	$2.21 \pm 0.01$	0.53
SDSS J235219.98-004855.7	0.437	$2.72 \pm 0.09$	$9.70 \pm 0.15$	0.43
SDSS J091515.64+055256.9	0.790	$2.62 \pm 0.04$	$2.55 \pm 0.10$	0.43
SDSS J104224.46+022225.0	0.668	$2.17 \pm 0.02$	$4.28 \pm 0.10$	0.84
SDSS J104630.88-010759.0	0.630	$2.66 \pm 0.05$	$3.20 \pm 0.12$	0.84
SDSS J105745.85-005818.6	0.655	$1.58 \pm 0.01$	$3.56 \pm 0.06$	0.53
SDSS J115027.99+025118.1	0.483	$1.62 \pm 0.01$	$2.10 \pm 0.06$	0.51
SDSS J132953.78+295140.0	0.862	$1.43 \pm 0.02$	$4.45 \pm 0.18$	0.35
SDSS J135342.06+262157.1	0.538	$1.26 \pm 0.01$	$1.90 \pm 0.04$	0.44

NOTE. — Column 2: spectroscopic redshift. Column 3: circularized effective radius. Column 4: Sérsic index. Column 5: axis ratio  $b/a$ . Upper and lower blocks represent sample 1 and sample 2, respectively.

TABLE 3  
PARAMETERS OF DOUBLE-SÉRSIC MODELS.

Object Name	$R_e$ (kpc)	$n$	$b/a$	light (%)
SDSS J011004.73+140933.0	$0.43 \pm 0.00$	$1.52 \pm 0.02$	0.38	56
	$2.06 \pm 0.01$	$0.57 \pm 0.01$	0.37	44
SDSS J014355.21+133451.4	$0.58 \pm 0.01$	$4.09 \pm 0.06$	0.42	76
	$1.00 \pm 0.01$	[0.50]	0.12	24
SDSS J081053.07+230443.7	$0.25 \pm 0.00$	$1.66 \pm 0.03$	0.53	40
	$1.71 \pm 0.01$	$0.82 \pm 0.01$	0.21	60
SDSS J084223.93+050223.4	$0.57 \pm 0.00$	$0.64 \pm 0.02$	0.36	35
	$1.65 \pm 0.01$	$0.86 \pm 0.01$	0.18	65
SDSS J115836.93+021535.1	$0.48 \pm 0.01$	$3.90 \pm 0.10$	0.54	61
	$3.03 \pm 0.02$	[0.50]	0.62	39
SDSS J121954.26+003025.2	$0.23 \pm 0.00$	$1.25 \pm 0.03$	1.00	27
	$1.63 \pm 0.01$	$1.66 \pm 0.02$	0.25	73
SDSS J155037.84+024746.5	$0.32 \pm 0.00$	$1.00 \pm 0.02$	0.75	27
	$1.67 \pm 0.01$	$1.20 \pm 0.01$	0.37	73
SDSS J235219.98-004855.7	$0.27 \pm 0.00$	$2.84 \pm 0.06$	0.75	47
	$2.32 \pm 0.01$	$0.58 \pm 0.01$	0.24	53

NOTE. — Column 2: circularized effective radius. Column 3: Sérsic index. Column 4: axis ratio  $b/a$ . Column 5: fraction of light from each component. As described in the text, for SDSS J014355.21+133451.4 and SDSS J115836.93+021535.1 we force  $n = 0.5$  for their second components. Notice that we allowed the centroids of the two components to float in the fits. Only the best-fit centroids of SDSS J011004.73+140933.0 have a large offset of  $\sim 0.1''$ . For the other seven galaxies, the two components essentially share the same centroid because the offset is less than the pixel scale (0.02'').

Stockton, A., Canalizo, G., & Maihara, T. 2004, *ApJ*, 605, 37  
 Stockton, A., McGrath, E., Canalizo, G., Iye, M., & Maihara, T. 2008, *ApJ*, 672, 146  
 Stockton, A., Shih, H.-Y., & Larson, K. 2010, *ApJ*, 709, L58  
 Stockton, A., Shih, H.-Y., Larson, K., & Mann, A. W. 2014, *ApJ*, 780, 134  
 Taylor, E. N., Franx, M., Glazebrook, K., et al. 2010, *ApJ*, 720, 723  
 Toft, S., Gallazzi, A., Zirm, A., et al. 2012, *ApJ*, 754, 3  
 Toft, S., van Dokkum, P., Franx, M., et al. 2007, *ApJ*, 671, 285  
 Trujillo, I., Cenarro, A. J., de Lorenzo-Cáceres, A., et al. 2009, *ApJ*, 692, L118  
 Trujillo, I., Conselice, C. J., Bundy, K., et al. 2007, *MNRAS*, 382, 109

Trujillo, I., Ferré-Mateu, A., Balcells, M., Vazdekis, A., & Sánchez-Blázquez, P. 2014, *ApJ*, 780, L20  
 Trujillo, I., Ferreras, I., & de La Rosa, I. G. 2011, *MNRAS*, 415, 3903  
 Trujillo, I., Förster Schreiber, N. M., Rudnick, G., et al. 2006, *ApJ*, 650, 18  
 van de Sande, J., Kriek, M., Franx, M., et al. 2013, *ApJ*, 771, 85  
 van der Wel, A., Rix, H.-W., Wuyts, S., et al. 2011, *ApJ*, 730, 38  
 van der Wel, A., Franx, M., van Dokkum, P. G., et al. 2014, *ApJ*, 788, 28  
 van Dokkum, P. G., Franx, M., Kriek, M., et al. 2008, *ApJ*, 677, L5  
 van Dokkum, P. G., Whitaker, K. E., Brammer, G., et al. 2010, *ApJ*, 709, 1018



TABLE 4  
STELLAR POPULATION PROPERTIES FROM FAST.

Object Name	Age <sub>0</sub> (Gyr)	$\tau$ (Gyr)	$\langle \text{Age} \rangle$ (Gyr)	[Z/H]	$A_V$ (mag)	$M_*$ ( $10^{11} M_\odot$ )
SDSS J011004.73+140933.0	$1.05^{+0.05}_{-0.02}$	$0.16^{+0.02}_{-0.01}$	$0.89^{+0.05}_{-0.03}$	0.4	$0.31^{+0.06}_{-0.08}$	$1.10^{+0.11}_{-0.07}$
SDSS J012942.10+132420.8 <sup>a</sup>	$1.45^{+0.25}_{-0.75}$	$0.16^{+0.08}_{-0.16}$	$1.29^{+0.26}_{-0.77}$	0.4	$0.00^{+0.53}_{-0.00}$	$0.43^{+0.05}_{-0.08}$
SDSS J014355.21+133451.4	$4.57^{+1.74}_{-2.87}$	$0.79^{+0.52}_{-0.37}$	$3.78^{+1.83}_{-2.78}$	0.0	$0.12^{+0.13}_{-0.12}$	$0.69^{+0.16}_{-0.34}$
SDSS J081053.07+230443.7 <sup>a</sup>	$1.05^{+0.65}_{-0.28}$	$0.13^{+0.40}_{-0.12}$	$0.92^{+2.78}_{-0.66}$	0.4	$0.33^{+1.12}_{-0.33}$	$0.63^{+0.49}_{-0.11}$
SDSS J084223.93+050223.4	$1.58^{+0.35}_{-0.35}$	$0.16^{+0.08}_{-0.16}$	$1.43^{+0.29}_{-0.39}$	0.4	$0.04^{+0.13}_{-0.04}$	$0.62^{+0.09}_{-0.12}$
SDSS J084616.69+052833.6	$1.14^{+0.55}_{-0.21}$	$0.13^{+0.06}_{-0.12}$	$1.02^{+0.55}_{-0.25}$	0.4	$0.19^{+0.29}_{-0.13}$	$0.69^{+0.38}_{-0.08}$
SDSS J101009.25+062324.8	$7.59^{+0.36}_{-1.42}$	$2.00^{+0.14}_{-0.55}$	$5.59^{+0.38}_{-1.32}$	0.0	$1.06^{+0.12}_{-0.15}$	$1.66^{+0.12}_{-0.25}$
SDSS J115836.93+021535.1	$5.01^{+2.57}_{-2.61}$	$0.79^{+0.49}_{-0.79}$	$4.21^{+2.62}_{-2.73}$	0.0	$0.08^{+0.18}_{-0.08}$	$1.02^{+0.29}_{-0.30}$
SDSS J121954.26+003025.2	$3.47^{+5.24}_{-2.27}$	$0.13^{+0.95}_{-0.12}$	$3.34^{+5.33}_{-2.27}$	0.0	$0.32^{+0.37}_{-0.29}$	$0.65^{+0.38}_{-0.29}$
SDSS J123106.94+053347.6	$3.47^{+0.80}_{-1.69}$	$0.63^{+0.30}_{-0.33}$	$2.84^{+0.85}_{-1.72}$	0.0	$0.61^{+0.16}_{-0.22}$	$1.58^{+0.28}_{-0.65}$
SDSS J124257.04+102400.7	$1.20^{+0.12}_{-0.08}$	$0.20^{+0.05}_{-0.03}$	$1.00^{+0.13}_{-0.09}$	0.0	$1.13^{+0.16}_{-0.09}$	$1.35^{+0.20}_{-0.12}$
SDSS J134412.30+010906.6	$7.59^{+0.36}_{-2.80}$	$1.58^{+0.46}_{-0.79}$	$6.00^{+0.58}_{-2.91}$	0.0	$1.28^{+0.19}_{-0.14}$	$2.51^{+0.24}_{-0.56}$
SDSS J155037.84+024746.5	$1.00^{+0.00}_{-0.00}$	$0.01^{+0.01}_{-0.00}$	$0.99^{+0.02}_{-0.00}$	0.4	$0.00^{+0.00}_{-0.00}$	$0.66^{+0.02}_{-0.00}$
SDSS J164916.12+294309.0	$0.95^{+0.07}_{-0.08}$	$0.06^{+0.04}_{-0.06}$	$0.89^{+0.08}_{-0.10}$	0.4	$0.00^{+0.01}_{-0.00}$	$0.48^{+0.01}_{-0.02}$
SDSS J235219.98-004855.7 <sup>a</sup>	$8.71^{+0.00}_{-7.84}$	$1.00^{+0.41}_{-1.00}$	$7.71^{+0.41}_{-7.71}$	0.0	$0.35^{+1.21}_{-0.35}$	$1.12^{+0.20}_{-0.74}$
SDSS J091515.64+055256.9 <sup>a</sup>	$6.61^{+0.00}_{-5.58}$	$0.00^{+0.91}_{-0.00}$	$6.60^{+0.91}_{-5.58}$	0.0	$0.08^{+0.55}_{-0.08}$	$1.66^{+0.25}_{-1.10}$
SDSS J104224.46+022225.0	$1.45^{+0.46}_{-0.22}$	$0.00^{+0.17}_{-0.00}$	$1.44^{+0.49}_{-0.22}$	0.4	$0.01^{+0.14}_{-0.01}$	$0.68^{+0.14}_{-0.07}$
SDSS J104630.88-010759.0	$2.00^{+4.17}_{-0.79}$	$0.25^{+0.68}_{-0.25}$	$1.74^{+4.23}_{-0.85}$	0.4	$0.29^{+0.49}_{-0.29}$	$0.68^{+0.70}_{-0.11}$
SDSS J105745.85-005818.6	$4.57^{+0.80}_{-2.17}$	$0.79^{+0.28}_{-0.75}$	$3.78^{+0.85}_{-2.30}$	0.0	$0.00^{+0.04}_{-0.00}$	$1.20^{+0.12}_{-0.31}$
SDSS J115027.99+025118.1	$3.80^{+4.52}_{-2.10}$	$0.79^{+2.23}_{-0.45}$	$3.01^{+5.03}_{-2.15}$	0.4	$0.48^{+0.69}_{-0.42}$	$0.43^{+0.35}_{-0.12}$
SDSS J132953.78+295140.0	$2.19^{+1.36}_{-1.23}$	$0.32^{+0.21}_{-0.31}$	$1.87^{+1.38}_{-1.27}$	0.0	$0.73^{+0.45}_{-0.43}$	$1.15^{+0.26}_{-0.44}$
SDSS J135342.06+262157.1	$5.75^{+2.19}_{-4.55}$	$0.79^{+0.49}_{-0.79}$	$4.96^{+2.24}_{-4.62}$	0.0	$0.76^{+0.58}_{-0.26}$	$1.62^{+0.42}_{-0.93}$

NOTE. — Column 2: the age since the onset (peak) of star formation. Column 3:  $e$ -folding timescale for the star formation rate. Column 4: the mean age of the stellar population, which is the age since one  $\tau$  after the onset of star formation ( $= \text{Age}_0 - \tau$ ). Column 5: metallicity. Column 5: magnitude of rest-frame visual extinction. Column 6: stellar mass. Upper and lower blocks represent sample 1 and sample 2, respectively.

The stellar populations of these four galaxies are only constrained by the photometry.

TABLE 5  
STELLAR POPULATION PROPERTIES, VELOCITY DISPERSIONS AND DYNAMICAL MASSES BASED ON PXP FULL-SPECTRUM FITS.

Object Name	$\langle \text{Age} \rangle_M$ (Gyr)	$\langle \text{Age} \rangle_L$ (Gyr)	$[\langle Z/H \rangle]_M$	$[\langle Z/H \rangle]_L$	$A_V$ (mag)	$M_*$ ( $10^{11} M_\odot$ )	$\sigma$ (km s <sup>-1</sup> )	$M_{\text{dyn}}^a$ ( $10^{11} M_\odot$ )	$M_{\text{dyn}}^b$ ( $10^{11} M_\odot$ )
SDSS J011004.73+140933.0	1.03	0.95	0.34	0.34	0.00	0.87	271±8	0.94±0.05	2.08±0.12
SDSS J014355.21+133451.4	8.15	6.71	-0.10	0.00	0.18	1.38	247±9	0.65±0.05	2.05±0.15
SDSS J084223.93+050223.4	3.18	2.59	0.14	0.22	0.06	1.11	268±5	1.18±0.04	2.29±0.08
SDSS J084616.69+052833.6	2.06	1.48	0.03	0.10	0.36	1.37	249±11	0.89±0.08	2.15±0.18
SDSS J101009.25+062324.8	5.56	4.20	0.05	0.14	0.28	1.20	142±14	0.34±0.07	0.66±0.13
SDSS J115836.93+021535.1	6.04	4.28	-0.01	-0.03	0.77	2.44	172±9	0.79±0.08	1.39±0.14
SDSS J123106.94+053347.6	2.55	1.85	0.13	0.22	0.29	1.22	261±7	0.90±0.05	2.24±0.11
SDSS J124257.04+102400.7	0.80	0.74	0.30	0.29	0.57	0.95	237±12	0.67±0.07	1.65±0.17
SDSS J155037.84+024746.5	3.34	1.93	0.22	0.31	0.00	0.63	227±9	0.88±0.07	1.27±0.10
SDSS J105745.85-005818.6	5.00	4.09	-0.03	-0.08	0.00	1.48	278±11	1.57±0.12	2.86±0.22

NOTE. — Column 2&3: mean mass-weighted and luminosity-weighted ages. Column 4&5: mean mass-weighted and luminosity-weighted metallicities. Column 6: magnitude of rest-frame visual extinction. Column 7: stellar mass. Column 8: velocity dispersion. Column 9&10: dynamical masses. Upper and lower blocks include objects from sample 1 and sample 2, respectively.

<sup>a</sup>Calculated from the virial relation  $M_{\text{dyn}} = \beta \sigma_e^2 R_e / G$ , with  $\beta = 5$ .

<sup>b</sup>Calculated from the virial relation, but with  $\beta = 6(R_e/3.185)^{-0.81}(M_*/10^{11})^{0.45}$ , following Peralta de Arriba et al. (2014), where  $R_e$  is in kpc and  $M_*$  is the stellar mass from column 3, corrected for the difference between our assumed Chabrier (2003) IMF and the Salpeter IMF assumed by Peralta de Arriba et al. (2014), following the equation 12 in Longhetti & Saracco (2009).

Wizinowich, P. L., Le Mignant, D., Bouchez, A. H., et al. 2006, PASP, 118,  
297

#### APPENDIX

We present all the 22 galaxy images and their corresponding GALFIT fits in Figure A1 and A2. The ten spectra we used for pPXF full-spectrum fits and their results are shown in Figure A3.

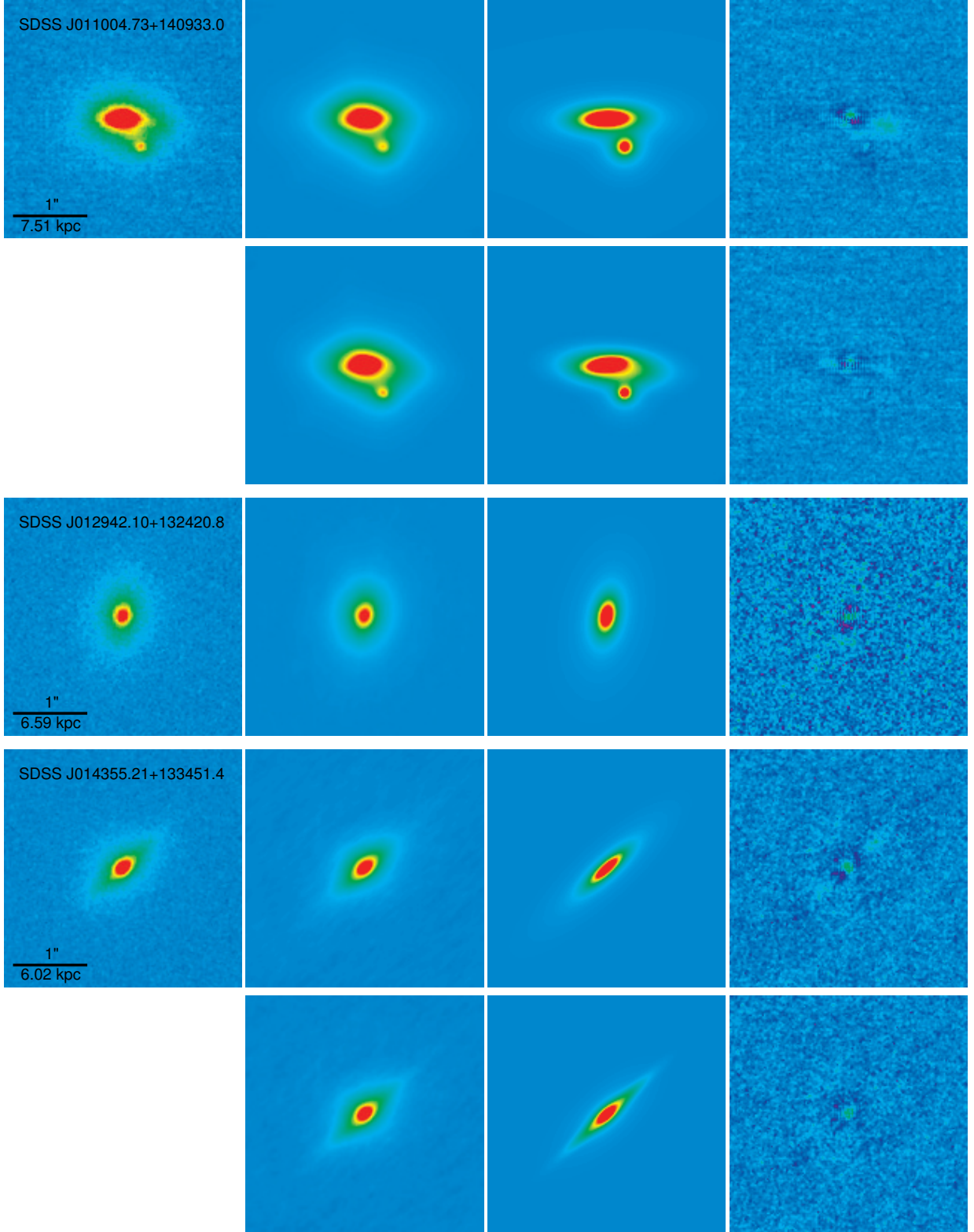


FIG. A1.— Keck LGSAO false-color images and model fits, where the first row of a object represents a one-component fit, and the second row (if exists) represents a two-component fit. For each galaxy, the panels from left to right show the original image, the best-fit model, the model without PSF convolution, and the residual. The images and models are in power-law scale in order to show the faint outer profiles of the galaxies. The residuals are in linear scale with a different contrast in order to show the small variations across the fields. An one-arcsecond scale and the corresponding physical length at the galaxy redshift is shown in the lower-left corner of every galaxy image. North is up and east to the left for all images. For SDSS J011004.73+140933.0, we include another Sérsic profile for the close companion.

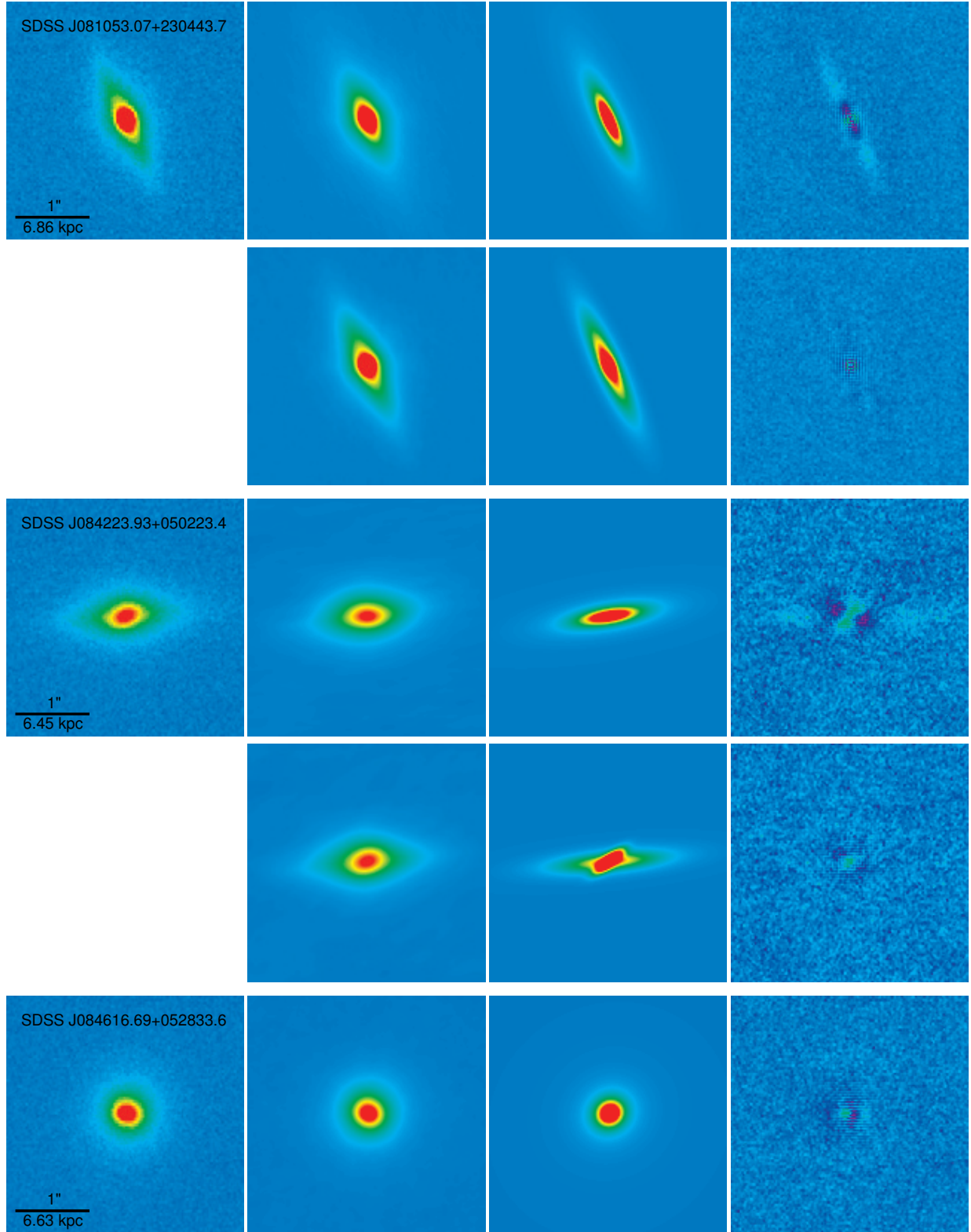


FIG. A1.— Continued. Notice that the PSF-deconvolved two-component model for SDSS J084223.93+050223.4 appears to be unphysical since the position angles of the two components do not align. However, we still keep this double-Sérsic model because the galaxy image shows that the inner isophotes are indeed not aligned with the outer ones. Also, this model does much reduce the residual.

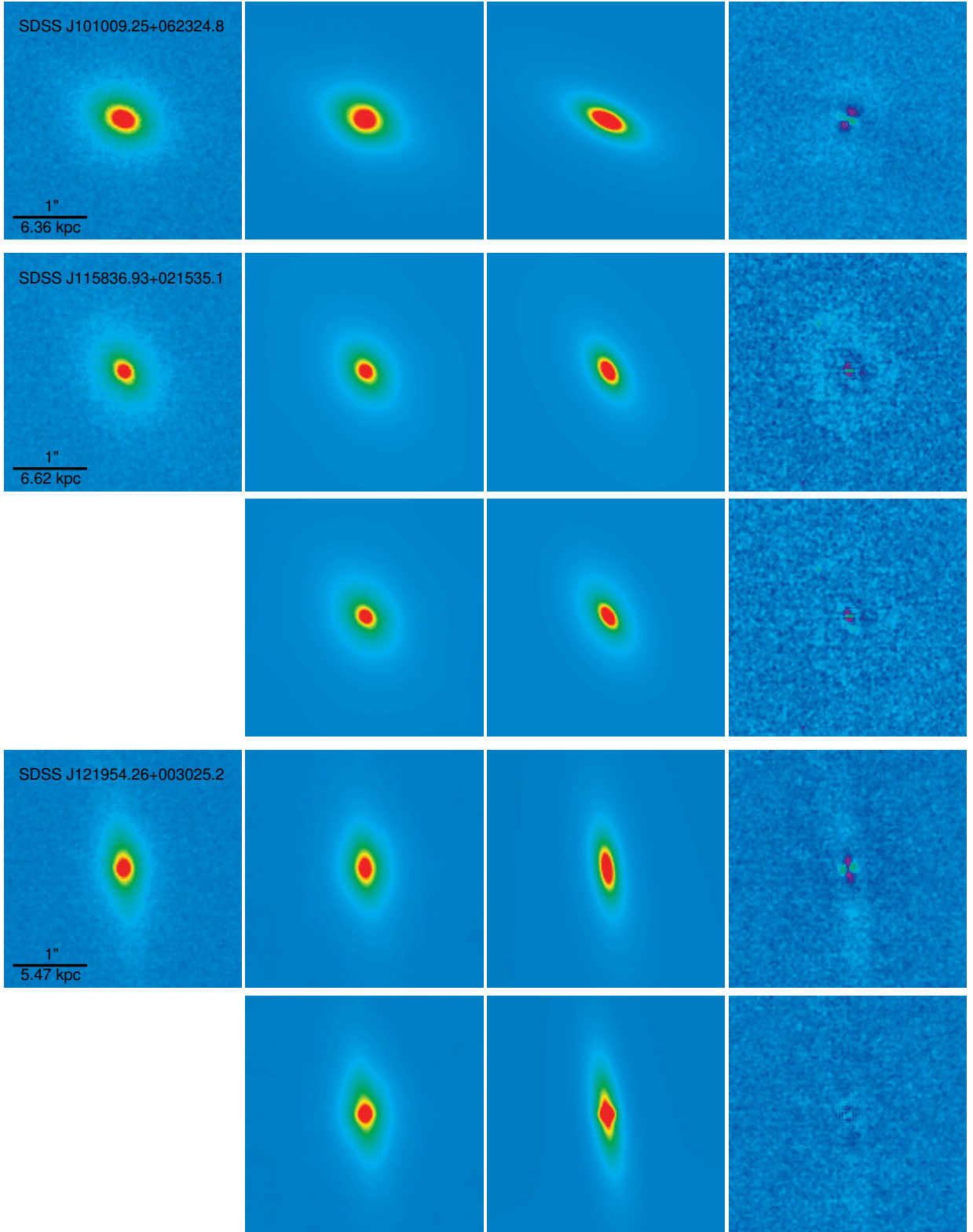


FIG. A1.— Continued.



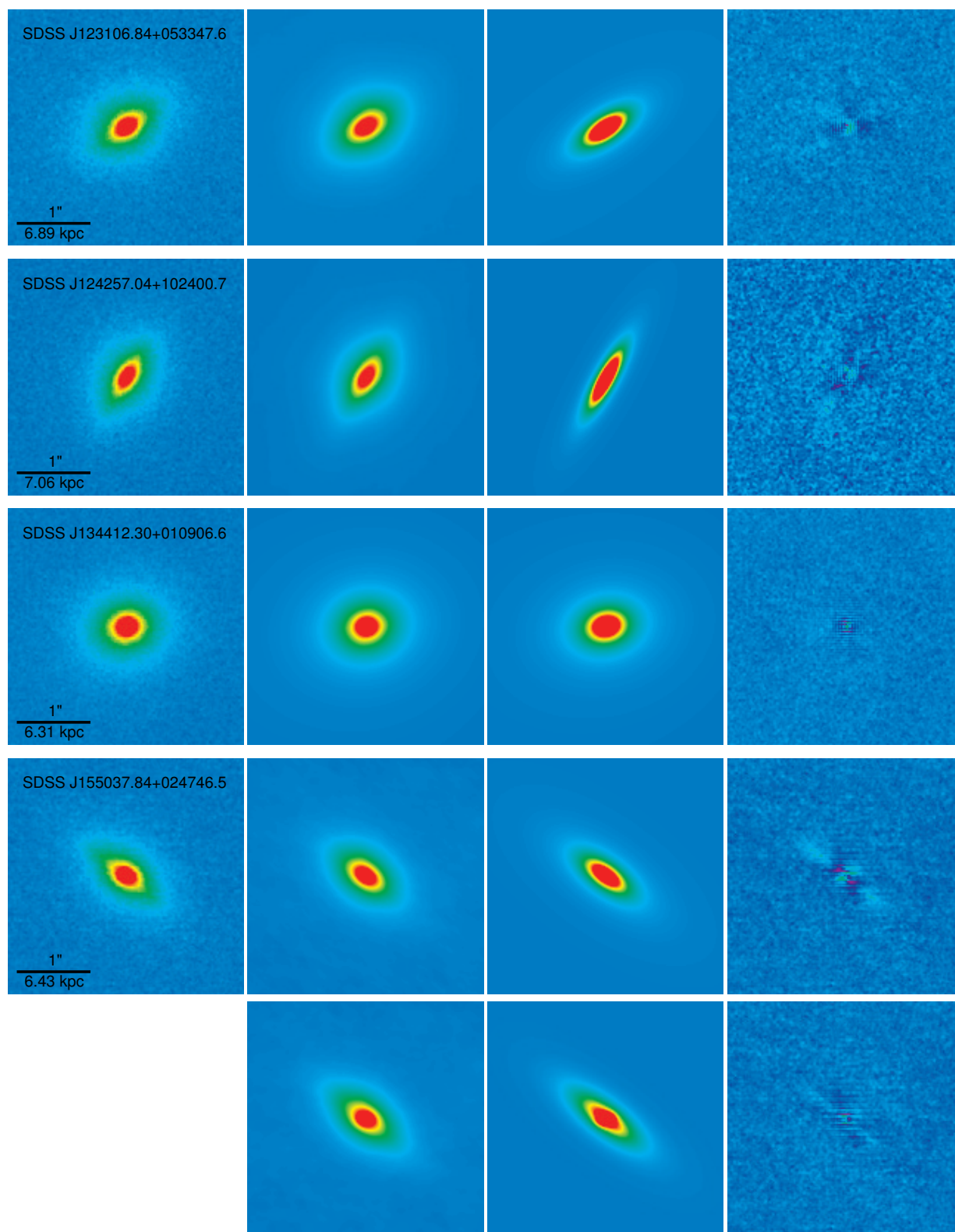


FIG. A1.— Continued.

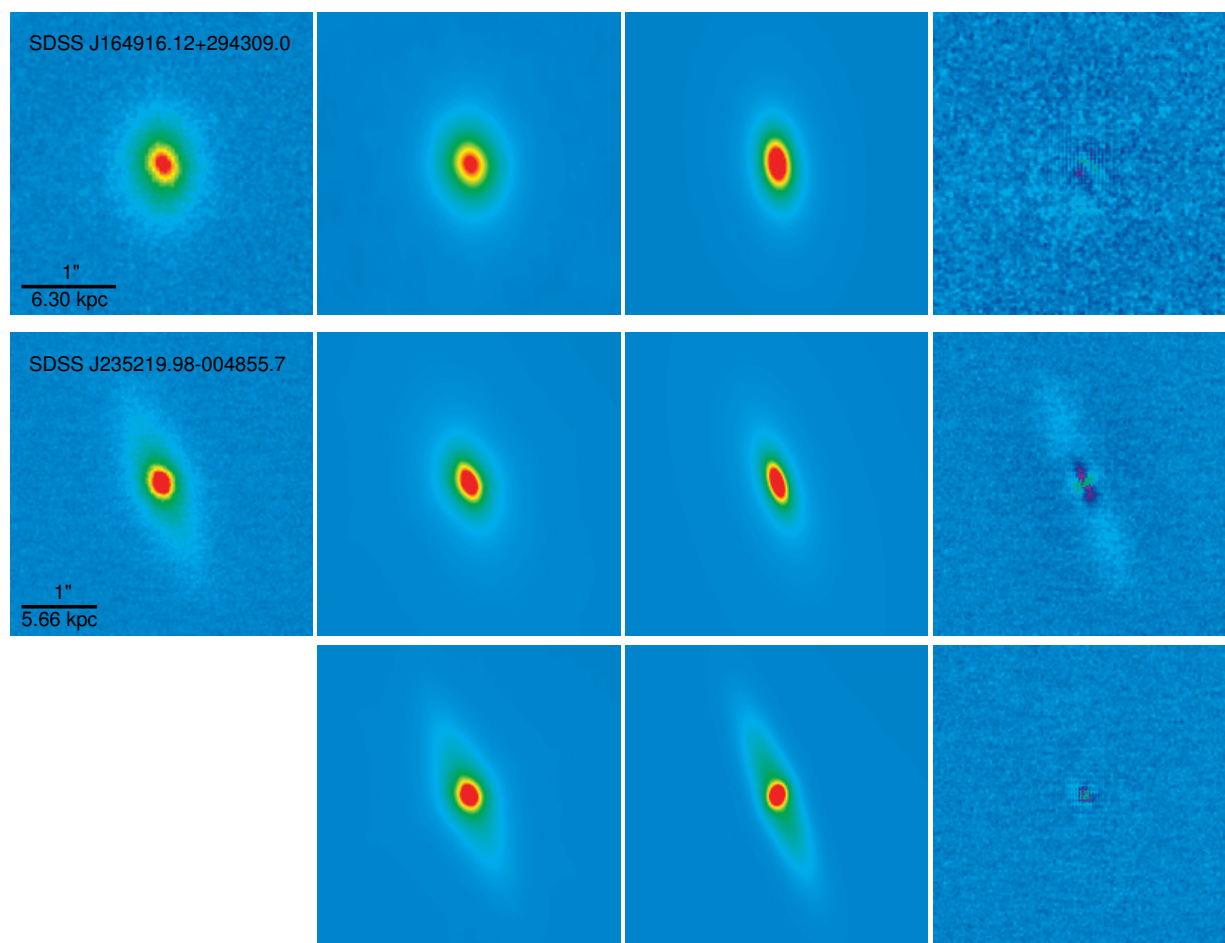


FIG. A1.— Continued.

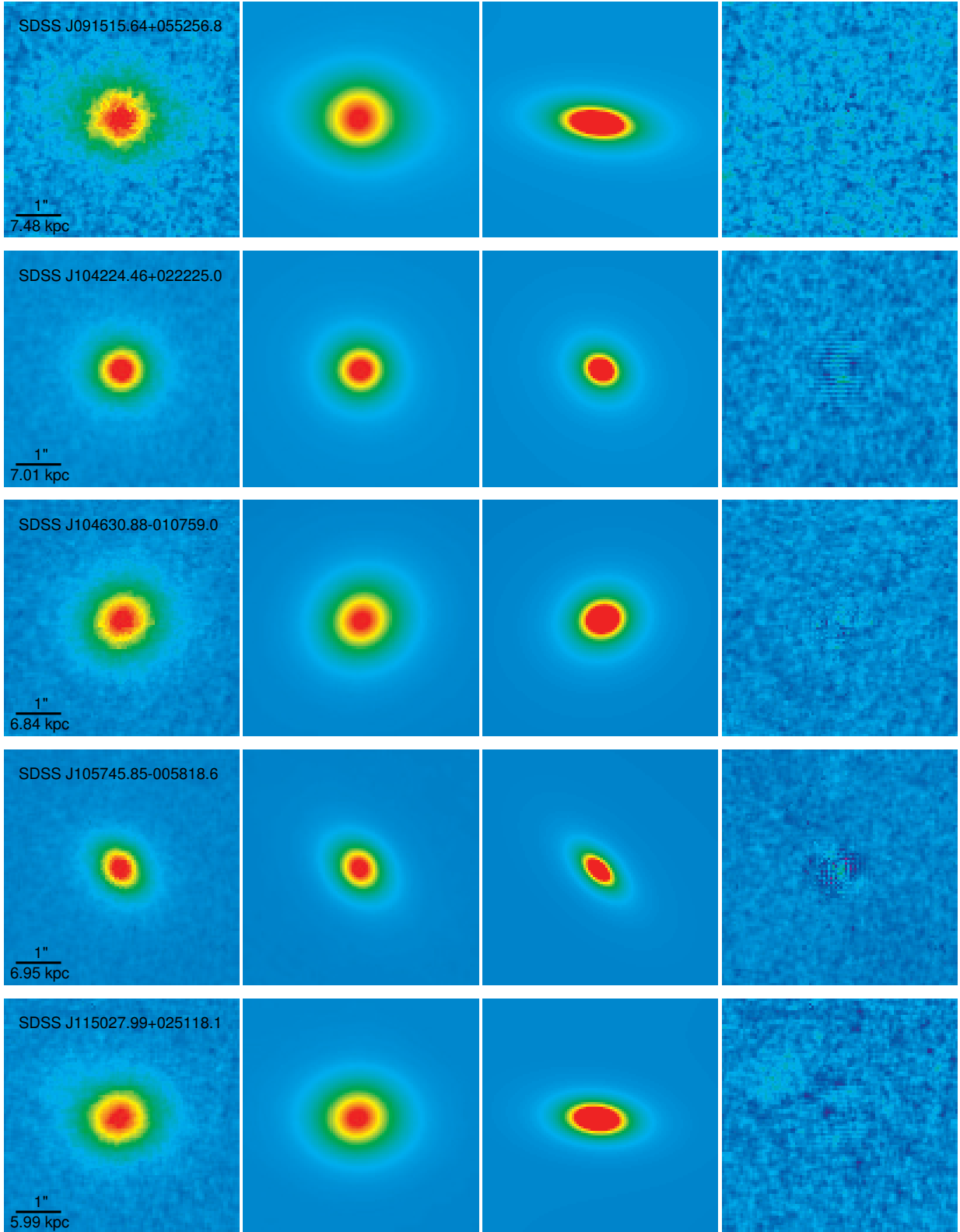


FIG. A2.— Subaru/FOCAS false-color images and model fits. For each galaxy, the panels from left to right show the original image, the best-fit model, the model without PSF convolution, and the residual. The images and models are in power-law scale in order to show the faint outer profiles of the galaxies. The residuals are in linear scale with a different contrast in order to show the small variations across the fields. An one-arcsecond scale and the corresponding physical length at the galaxy redshift is shown in the lower-left corner of every galaxy image. North is up and east to the left for all images.



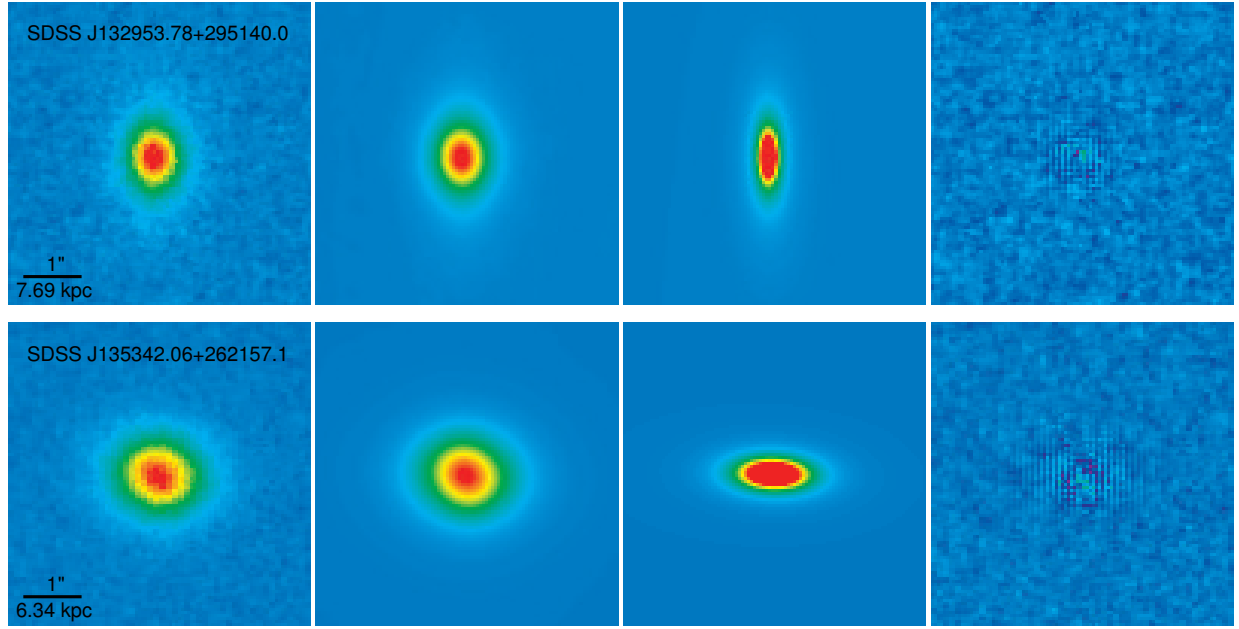


FIG. A2.— Continued.

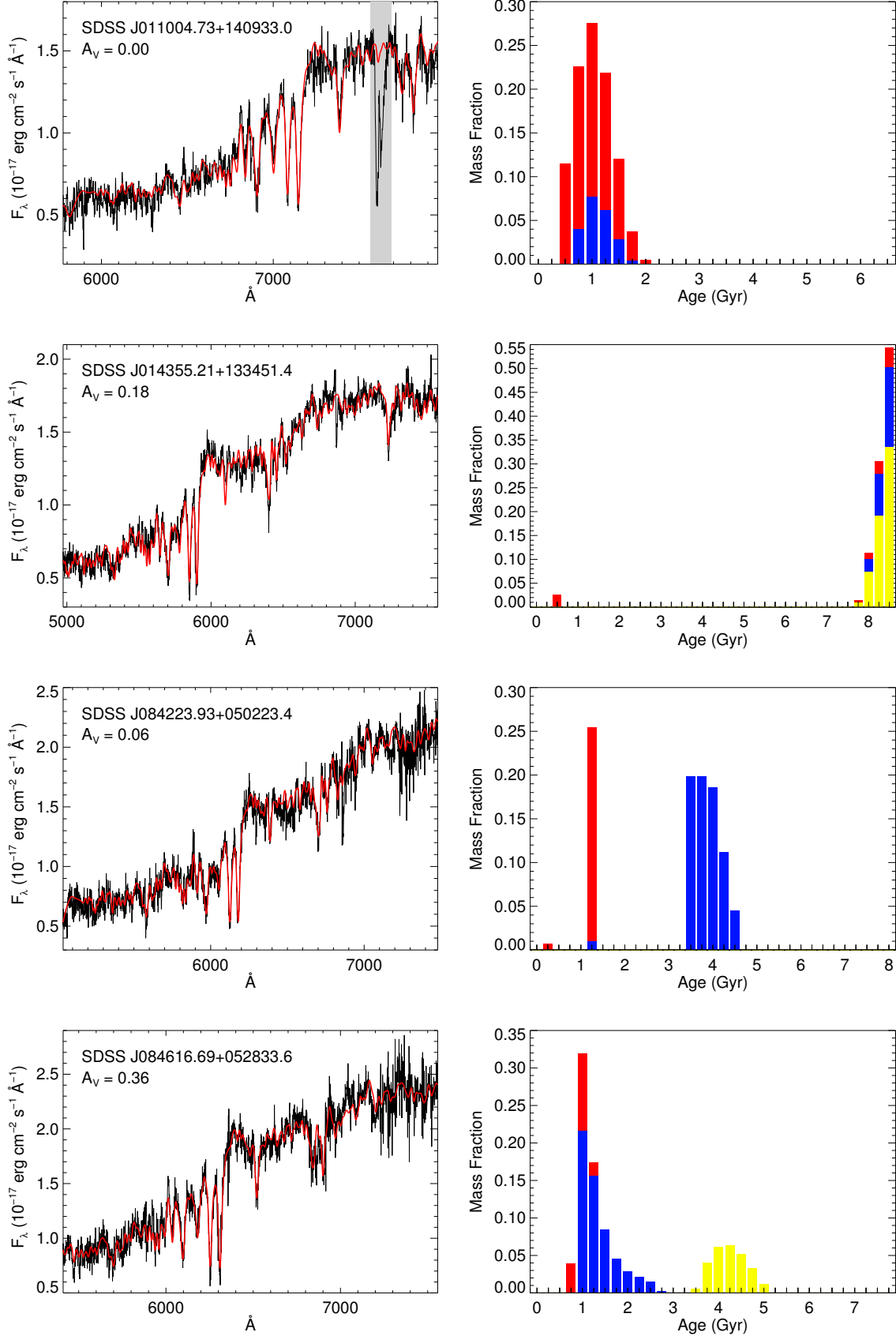


FIG. A3.— Left panels: Full-spectrum fits using pPXF, where black lines are the observed spectra and red lines are the best-fit models. Gray areas represent the masks of bad pixels. Right panels: The best-fit stellar populations, illustrated by the fraction of star formation at a given look-back time. Red, blue and yellow portions of the bars represent the additive mass fractions with metallicity  $[Z/H]$  of 0.4, 0.0 and -0.4, respectively (i.e., the mass fraction at a given time is represented by the height of the corresponding column, which is the sum of red, blue and yellow portions of the bar). The sum of all the columns equals one. The last age grid is the oldest age younger than the age of universe at the galaxy redshift.

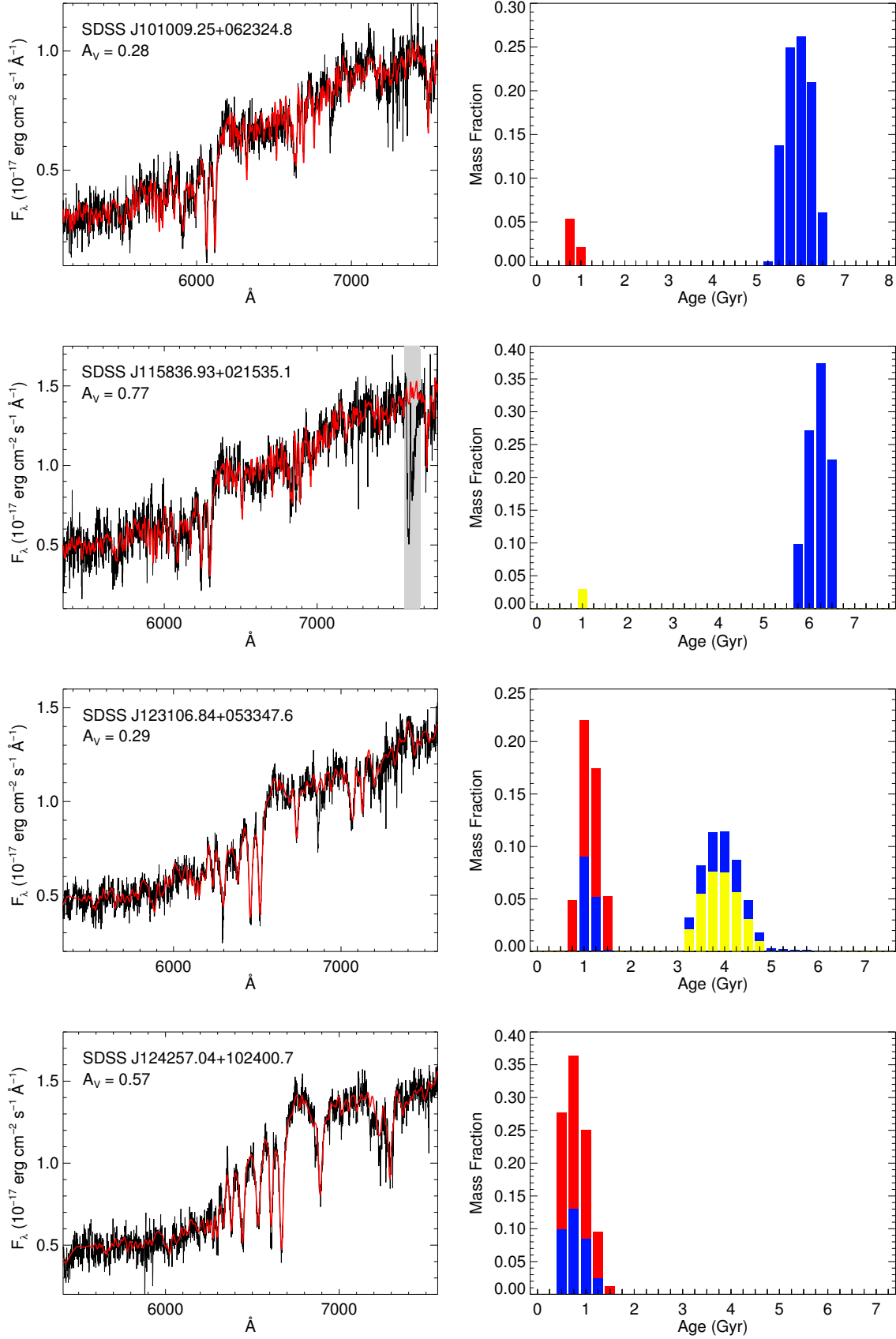


FIG. A3.— Continued.

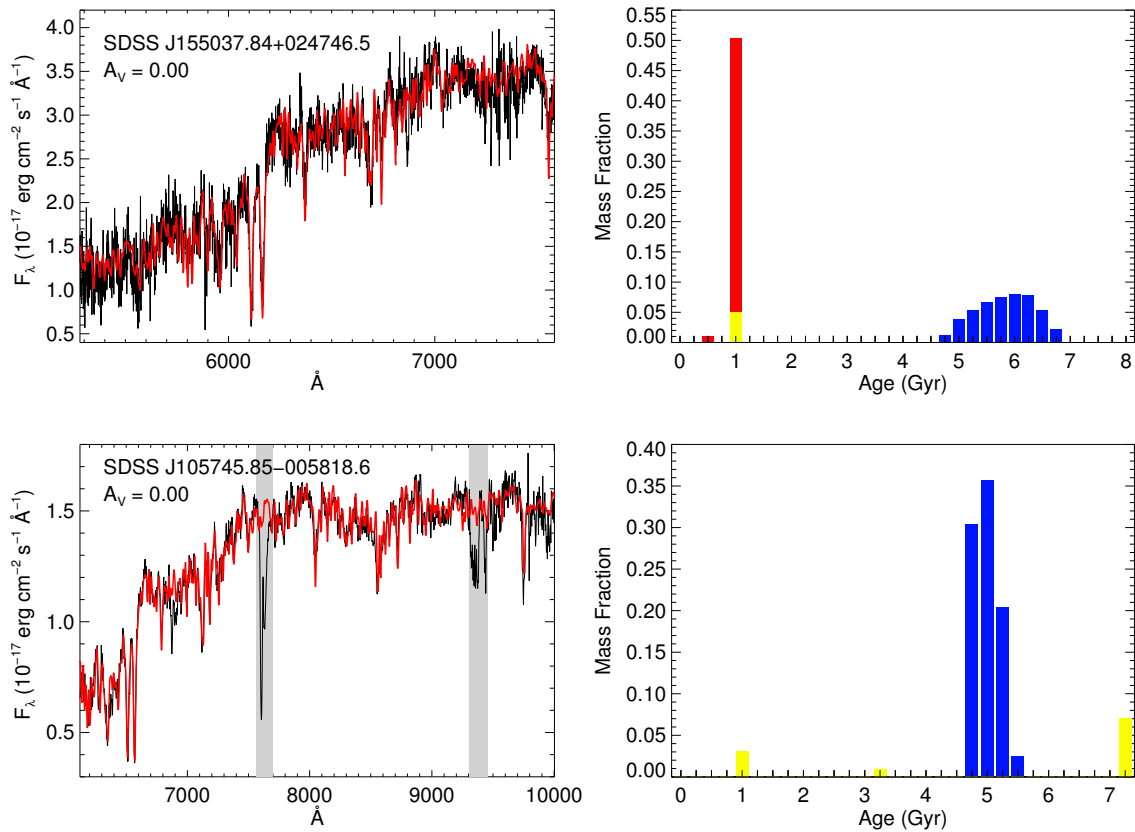


FIG. A3.— Continued.